



Modeling ash deposition and shedding during oxy-combustion of coal/rice husk blends at 70% inlet O₂

Gautham Krishnamoorthy¹

Received: 31 May 2022 / Revised: 21 September 2022 / Accepted: 6 March 2023
© The Author(s) 2023

Abstract

Co-firing rice husk (RH) and coal with carbon capture using oxy-combustion presents a net carbon negative energy production opportunity. In addition, the high fusion temperature of the non-sticky, silica rich, RH can mitigate ash deposition as well as promote shedding of deposits. To identify the optimum operating conditions, fuel particle sizes, and blend ratios that minimize ash deposition, a Computational Fluid Dynamic methodology with add-on ash deposition and shedding models were employed to predict outer ash deposition and shedding rates during co-combustion of coal/RH in AIR and O₂/CO₂ (70/30 vol%, OXY70) oxidizer compositions. After ensuring that the fly-ash particle size distributions and particle Stokes numbers near the deposition surface were accurately represented (to model impaction), appropriate models for coal ash and RH ash viscosities that were accurate in the temperature region (1200–1300 K) of interest in this study were identified. A particle viscosity and kinetic energy (PKE) based capture criterion was enforced to model the ash capture. An erosion/shedding criterion that takes the deposit melt fraction and the energy consumed during particle impact into account was also implemented. Deposition rate predictions as well as the deposition rate enhancement (OXY70/AIR) were in good agreement with measured values. While the OXY70 scenario was associated with a significant reduction (60%–70%) in flue gas velocities, it also resulted in larger fly-ash particles. As a result, the PKE distributions of the erosive RH ash were similar in both scenarios and resulted in similar shedding rates.

Keywords CFD · Oxy-Combustion · Ash Deposition · Shedding · Co-firing

Abbreviations

D	Diameter, m
e	Erosivity
E	Energy, J
Re	Reynolds number
Stk	Stokes Number
T	Temperature, K
u	Velocity, m/s

Greek symbols

γ	Surface tension, N/m
η	Efficiency
ρ	Density, kg/m ³
μ	Viscosity, kg/m s
ξ_s	Molten slag fraction

Subscripts

p	Denotes particle
-----	------------------

1 Introduction

1.1 Rice husk/coal co-combustion

Co-firing rice husk (RH)—a carbon-neutral renewable energy source, and coal with carbon capture using oxy-combustion presents a *net carbon negative* energy production opportunity. RH has a heating value comparable to that of lignite, has a high ash content (13 wt%–29 wt%) that is rich in silica (87 wt%–97 wt%). In spite of this, coal/RH co-firing scenarios appear to reduce fouling propensities due to the formation of high-fusion-temperature, non-sticky rice husk ash along with the capture of fouling-inducing species from coal by the RH ash (Wu et al. 2018, 2019). In addition to these fuel-ash interactions, the ash from co-firing RH and coal were found to possess crystalline structures similar to that of coal ash. Despite these advantages, operating at an optimum blend ratio (Coal: RH) is also important. RH-Coal

✉ Gautham Krishnamoorthy
gautham.krishnamoorthy@engr.und.edu

¹ Department of Chemical Engineering, UPSON II Room 365, 241 Centennial Drive, University of North Dakota, Grand Forks, ND 58202-7101, USA

co-combustion characteristics such as ignition time and temperature, burnout time, ash transformation characteristics and ash fusion temperature at different blending ratios have been investigated by Yang et al. (2022) and Wang et al. (2020a). Yang et al. (2022) recommended a blend ratio (Zhungdong coal: RH hydrochar) of at least 7:3 to avail the benefits of co-combustion. Similarly, Chao et al. (2008) and Kwong et al. (2007) identified 10 wt%–30 wt% of RH in the fuel feed as an optimum range for minimizing pollutant emissions per unit energy output.

1.2 Ash deposition in first generation, atmospheric pressure oxy-combustion systems

The primary objectives of *first generation* oxy-fuel combustion systems were to match the heat flux and temperature profiles associated with combustion in air. This was typically accomplished by maintaining 27 vol%–32 vol% O₂ (with the remainder being CO₂ + H₂O) in the oxidizer stream and was accompanied by a 25%–30% reduction in the volumetric flow rate of the gases through the combustor with a corresponding decrease in the gas and particle velocities. However, the resulting increase in particle residence time also promoted physio-chemical interactions among the fly-ash and resulted in a PSD shift to larger diameters in comparison to air firing. The net result of both these changes was either an increase/decrease in ash deposition rates under oxy-firing in comparison to firing in air due to wide variations in the fuel, reactor geometry and probe temperatures across the investigated scenarios. Nonetheless, there appears to be a somewhat of a general consensus regarding the aerodynamic effects associated with the deposition process in these first-generation, atmospheric pressure systems as summarized in a recent review by Yu et al. (2021).

1.3 Ash deposition in second generation, atmospheric pressure oxy-combustion

The main objectives of second generation, atmospheric pressure oxy-combustion systems is to improve the economic feasibility of oxy-combustion cycles by minimizing the costs associated with air-separation, flue gas recycle and CO₂ compression and storage. The use of a highly oxygen enriched oxidizer stream (up to 70%–80% O₂ by volume) and the associated 60%–70% reduction in the volume of flue gas circulating through the combustor in comparison to combustion in air shows significant potential for efficiency improvements to be realized (Gopan et al. 2020). Again, these conditions result in: a corresponding reduction in the combustor gas velocities, an associated increase in ash concentrations, temperatures and particle residence times at thermal loads identical to combustion in air (Wang et al. 2019a, b). These factors in turn alter the particle size

distribution (PSD) of the fly-ash particles by increasing their molten fraction, promoting mineral interactions, and providing more opportunities for physiochemical transformations. Studies from Prof. Wendt's group at the University of Utah have indeed shown the PSD of the fly-ash particles to shift towards larger size ranges in these highly oxygen enriched environments (Wu et al. 2019; Wang 2019). Consequently, Prof. Wendt's group (Wang et al. 2019a, b; Wu et al. 2019; Wang 2019, Zhan et al. 2016) found an enhancement in ash deposition rates in all of the second generation oxygen enriched conditions (when compared to combustion in air) encompassing a wide range of fuel-types including coal/RH blends and attributed this to both aerodynamic and chemical effects. Since second generation oxy-combustion systems also result in higher temperatures within the combustor, this causes a corresponding variation in the ash properties (viscosity, surface tension and molten fraction or thermal effects) thereby influencing deposition/sticking propensities. However, the relative influences of the aerodynamic, chemical and thermal effects on the ash deposition rates have not been quantified and is a void this paper will attempt to fill. An additional phenomenon that has been noted in these systems is that if the RH fuel PSD is larger than the coal PSD, the resulting larger-sized RH ash particles under the right aerodynamic conditions can induce shedding of the ash deposits (Wu et al. 2019; Wang et al. 2019b). A second goal of this manuscript is implement and evaluate the performance of a recently proposed erosion/shedding model that takes the deposit melt fraction and the energy consumed during particle impact into account to discern if the observed shedding characteristics can be replicated in the simulations.

1.4 Objectives of this study

The primary objectives of this study is to discern the causative mechanisms behind the observed deposition/shedding behavior observed by Wu et al. (2019) in the two Coal/RH co-firing scenarios (AIR and O₂/CO₂ (70/30 vol%, OXY70) oxidizer composition). In particular, we seek answers to the following questions:

- (1) Given that: the RH fly-ash was larger in size and more porous than the coal fly-ash in both (AIR and OXY70) scenarios and there was a three-fold variation in flue gas volumetric flow rate between the two scenarios, what is the net result of these variations on the fly-ash impaction rates/efficiencies on the deposit probe?
- (2) Given that: the observed variations in the fly-ash characteristics stated above (PSD, density and velocity) directly impact particle kinetic energy (PKE), and the ash compositional and temperature variations (between AIR and OXY70) impact surface tension and particle viscosity, what is the net result of these variations on

the fly-ash capture and collection efficiencies on the deposit probe?

- (3) Can the deposit melt fraction (estimated by Wu et al. 2019) and the energy consumed during particle impact (obtained by accurate resolution of the PKE) be taken into account to develop an erosion/shedding criterion that faithfully reproduces the erosion/shedding characteristics observed in the experiments?

A Computational Fluid Dynamic (CFD) methodology with the following add-on modules were utilized in this study to answer the aforementioned questions:

- (1) *Accurate radiative property models for gases and particles* OXY70 combustion scenarios are characterized by low H₂O/CO₂ ratios and are dominated by gas radiation due to the high concentrations of radiatively participating gases. To ensure that the gas temperatures are being accurately represented, validated models for the gas radiative properties (Krishnamoorthy 2013) and fly-ash (Krishnamoorthy and Wolf 2015) were implemented as user-defined functions (UDF) in the CFD code ANSYS FLUENT (ANSYS Fluent Theory Guide 2020).
- (2) *PKE-critical viscosity based ash capture criterion* A PKE-critical viscosity based ash capture criterion that was originally developed for silica rich soda lime glasses but whose validity for biomass ashes has been established was also implemented as UDF. This was done after ensuring that the boundary layer surrounding the ash probe was of sufficient resolution (as per

the criteria set forth in Weber et al. 2013) to ensure accurate particle impaction predictions i.e., we ensured that the size (Δ) of the numerical cells adjacent to the cylindrical probe of diameter D was well within the constraint $\Delta \leq 0.3240D/4\sqrt{Re}$.

- (3) *Erosion or shedding model* The estimated deposit melt fraction and the energy consumed during particle impact were then taken into account to develop an erosion/shedding criterion based on the framework provided by Zhou and Hu (2021) that was implemented and evaluated as an additional UDF.

2 Method

2.1 Combustion simulation and validation

The 3D geometry representation of the down flow laboratory combustor (oxyfuel combustor or OFC) at the University of Utah that was simulated in this study is shown in Fig. 1a. The geometry was meshed with 1.1 M cells after ensuring grid convergence of the temperature and velocity fields at this level of refinement with particular care to ensure that the boundary layer surrounding the probe was adequately resolved as mentioned above. Table 1 summarizes the proximate and ultimate analysis of the fuels simulated in this study which is based on the experimental information reported in Wu et al. (2019) and the key flow rates corresponding to the experimental scenarios that were investigated are reported in Table 2. Table 2 shows that the simulated gas flow rates agree well with experimental

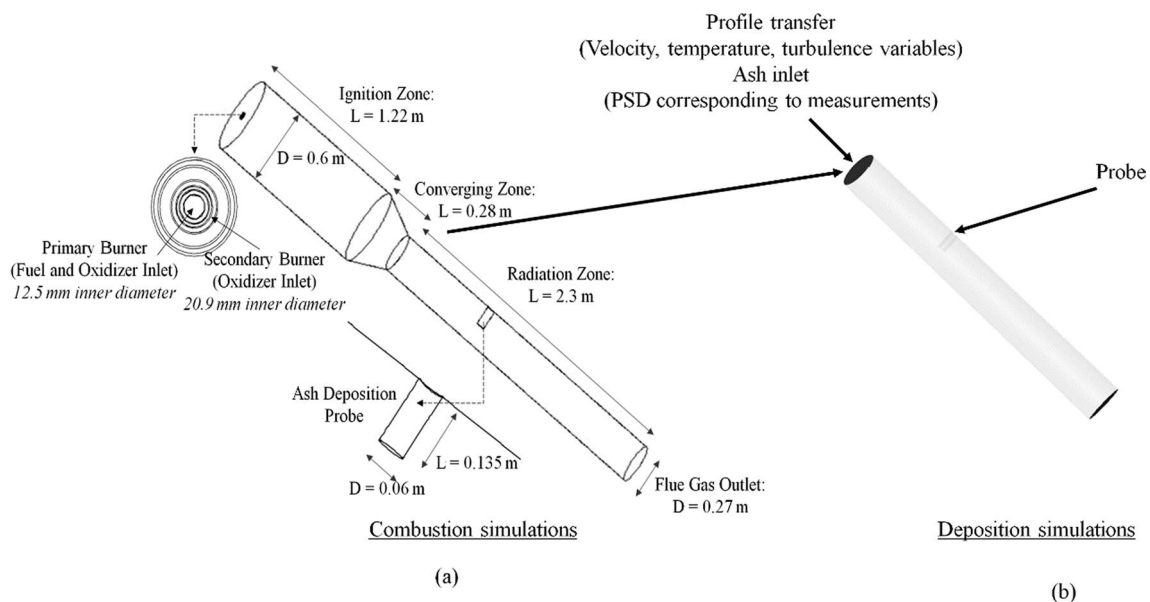


Fig. 1 Geometric details of the down flow OFC combustor. **a** Domain for combustion simulations **b** Domain (radiation zone only) for the ash deposition simulations

Table 1 Proximate and ultimate analysis of the fuels simulated in this study (based on Wu et al. 2019)

Sample	Proximate analysis (wt%)		Ultimate analysis (wt%, dry ash free)	
Rice Husk	Fixed Carbon	13.8	C	35.8
	Volatiles	60.8	H	5.1
	Ash	15.1	N	0.4
	Moisture	10.4	S	0.1
	HHV (MJ/kg)	14.6	O	33.1
Coal	Fixed Carbon	46.3	C	64.1
	Volatiles	32.2	H	4.3
	Ash	14.8	N	0.8
	Moisture	6.7	S	1.1
	HHV (MJ/kg)	28.0	O	8.2

Table 2 Key experimental conditions simulated in this study (based on Wu et al. 2019)

Parameter	84 wt% Coal–16% RH	
	OXY70	AIR
Energy input (kW)	27	27
Rice husk feeding rate (kg/h)	0.63	0.63
Coal feeding rate (kg/h)	3.28	3.28
Simulated Gas flow rate (m ³ /h) (experimental estimates from Wu et al. (2019) reported in brackets)	9 (9)	29 (26)
O ₂ fraction in dry flue gas (vol%)	3	3

estimates across both scenarios providing us with an initial measure of validation. The walls of the ignition zone (Fig. 1a) were set to a temperature of 1250 K. The homogeneous gaseous combustion reactions were simulated using a two-step mechanism with: CO produced during devolatilization followed by its oxidation to CO₂ during the second reaction. The particle tracking was accomplished in a Lagrangian reference frame where the particle trajectory was carried out by taking into account various forces such as discrete phase inertia, hydrodynamic drag, and the force of gravity as follows:

$$\frac{d\bar{u}_p}{dt} = F_D(\bar{u} - \bar{u}_p) + \frac{\bar{g}(\rho_p - \rho)}{\rho_p} \quad (1)$$

$F_D(\bar{u} - \bar{u}_p)$ represents the drag force per unit particle mass and F_D and was calculated as:

$$F_D = \frac{18\mu}{\rho_p d_p^2} \frac{C_D \text{Re}}{24} \quad (2)$$

here, \bar{u} is the fluid phase velocity, \bar{u}_p is the particle velocity, μ is the molecular viscosity of the fluid, ρ is the fluid density, ρ_p is the particle density, and d_p is the particle diameter. The particle Reynolds number dependent drag coefficient C_D was computed using the Morsi and Alexander model (ANSYS FLUENT 2020). After the completion of the combustion process, the heating and cooling of an inert ash particle was accomplished using a simplified heat balance to relate the particle temperature $T_p(t)$ to the convective heat transfer and the absorption/emission of radiation at the particle surface as follows:

$$m_p c_p \frac{dT_p}{dt} = hA_p(T_\infty - T_p) + \epsilon_p A_p \sigma_{SB} (\theta_R^4 - T_p^4) \quad (3)$$

here m_p is the mass of the particle, c_p is the heat capacity of the particle, h is the convective heat transfer coefficient, A_p is the surface area of the particle, T_∞ is the local temperature of the continuous phase, ϵ_p is the particle emissivity, σ_{SB} is the Stefan-Boltzmann constant ($5.67 \times 10^{-8} \text{ W/m}^2 \text{ K}^4$), and θ_R is the radiation temperature. The effects of turbulence fluctuations on the impaction and deposition process was accounted for by averaging the impaction and deposition rates across 100 particle tracking calculations for each scenario. However, the impaction and deposition rates did not vary significantly across the particle tracking calculations due to the prevalence of streamlined flow conditions with very little vorticity in the vicinity of the probe. This has also been ascertained via high-fidelity, scale resolving simulations at similar flow conditions in this furnace by Zhou (2019). Table 3 provides a complete summary of the various modeling options invoked in this study. Also referenced are additional radiative property modules that were developed and utilized in this study as User-Defined Functions to predict heat transfer accurately in the low H₂O/CO₂ environments corresponding to the OXY70 conditions. It is important to note that the use of a kinetic/diffusion model for char oxidation successfully replicates the changes in combustion regimes with fuel particle size variations. In general, combustion in larger particles are diffusion controlled whereas those in small particles are kinetically controlled. This behavior has also been observed in coal-RH blends by Kwong et al. (2007).

No unburnt carbon was noted in the probe ash deposits in the experiments (Wu et al. 2018) indicating completion of the char oxidation process before the particles reach the probe. This was successfully replicated in the simulations predictions shown in Fig. 2 where regions of carbon burnout are shown. Also shown (for comparative purposes only) the corresponding carbon burnout regions for the coal (only) combustion scenario reported in Wu et al. (2019). Coal and the 84 wt% coal–16 wt% RH blend result in similar ignition and combustion characteristics which is in agreement

Table 3 A summary of the combustion modeling options utilized in this study

Physics being modeled	Modeling option
Particle devolatilization (heterogeneous)	Constant rate (50, 1/s)
Char oxidation (heterogeneous)	Kinetic/Diffusion Limited
Volatile combustion (homogeneous) to form products: CO, H ₂ O, N ₂ , SO ₂	Finite rate/Eddy dissipation
CO oxidation to form CO ₂ (homogeneous)	Finite rate/Eddy dissipation
Turbulence	Realizable k-epsilon
Particle Drag law	Morsi-alexander
Model describing radiative transport	Discrete Ordinates
Particle radiative property	Variable K _{abs} and K _{scat} (Krishnamoorthy and Wolf 2015)*
Particle scattering phase function	Anisotropic (forward scattering)
Gas-phase radiative property	Perry (5gg) (Krishnamoorthy 2013)*

*These models were implemented as User-Defined Functions (UDFs) in ANSYS FLUENT

with the results reported in Yang et al. (2022) and Wang et al. (2020a) for coal-RH blends at similar ratios. However, a slightly earlier onset of burnout prediction (closer to the burner) is noted in the OXY70 scenarios as a result of higher oxidizer O₂ concentrations. Again, these results are comparable to those of Wang et al. (2020a) where a significant reduction in ignition delay and ignition temperature was

noted for coal-RH blends at higher oxidizer O₂ concentrations which could be attributed to result from the increased thermal (higher temperatures) and mass diffusion (higher O₂ concentrations) in the OXY70 scenario.

While temperature measurements for this coal-RH firing scenario was not readily available, a wide range of fuel types have been investigated within this combustor, at identical

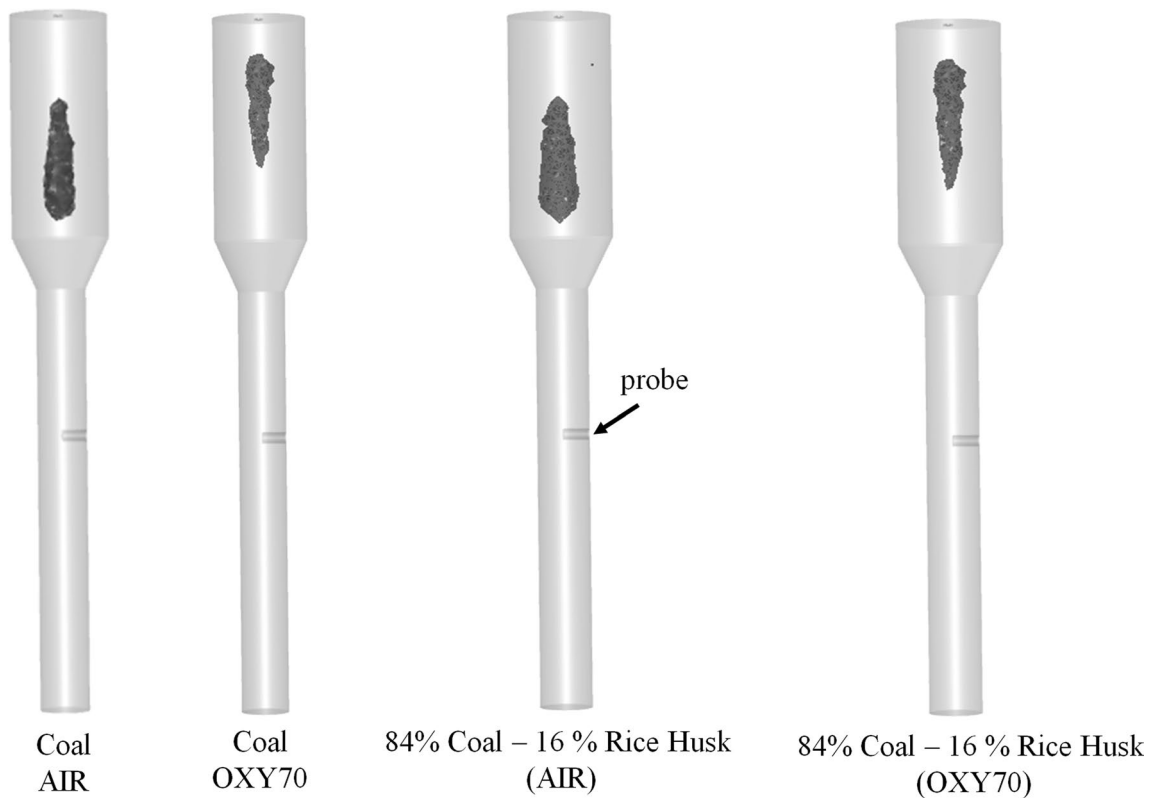


Fig. 2 Regions of carbon burnout. Complete carbon burnout is predicted in the ignition zone (wide section) before reaching the probe (indicated by arrow)

power outputs (27 kW). Since most of the firing scenarios (involving various fuel types) resulted in complete combustion by the time the gases reached the probe, they all resulted in similar gas temperatures (1150–1250 K) near the deposit probe as reported in previous studies (Wang 2019; Fakourian et al. 2021). The predicted gas temperature near the deposit probe in this study were 1270 and 1280 K respectively for the AIR and OXY70 scenario.

The measured fly-ash PSD from Wu et al. (2019) that have been fit to a Rosin–Rammler (RR) distribution function are shown in Fig. 3. The functional form representing

the RR distribution function are also shown in Fig. 3 with Y_d representing the fraction of mass that is greater than a particle diameter d_p , mean diameter ($d_{p,mean}$). An observed increase in particle sizes when switching from the AIR to OXY70 scenarios is captured in the $d_{p,mean}$ of the RR distribution for all fuels. A weighted averaging of the individual coal ash and RH fly-ash PSD from Figs. 3a-d was performed to estimate the fly-ash PSD of the 84% coal–16% RH fly-ash blend. These are shown are RR in Figs. 3e and f and are shown to compare with the measured fly-ash PSD indicating that modeling the fly-ash PSD of

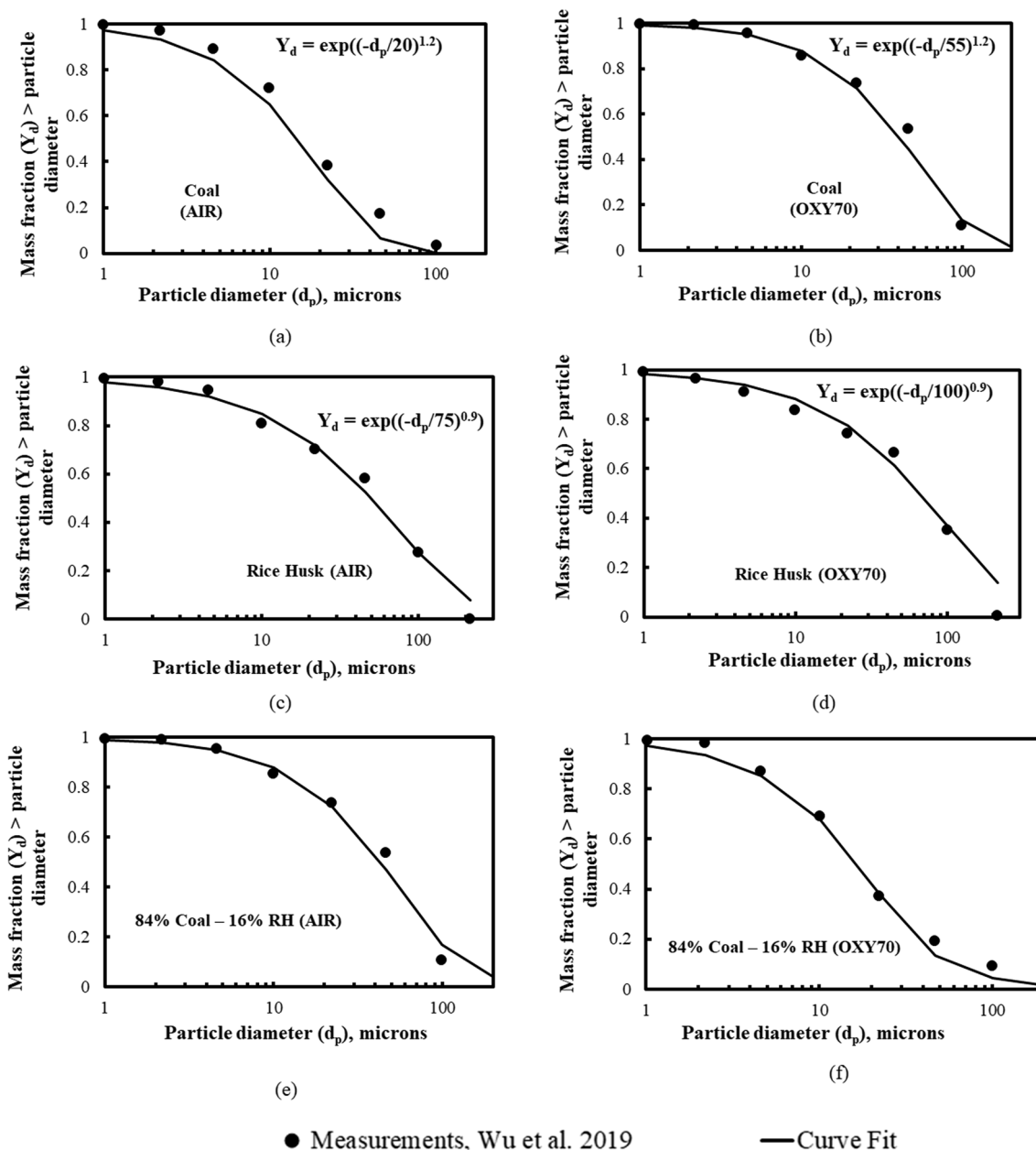


Fig. 3 The measured and modeled particle size distribution (PSD) of the fly-ash particles near the deposit probe (shown as a bold line). **a** Coal (AIR) **b** Coal (OXY70) **c** RH (AIR) **d** RH (OXY70) **e** 84% Coal–16% RH (AIR) **f** 84% Coal–16% RH (OXY70)

the individual fuels as evolving independent of each other without any physical interactions in the blended fuel scenario is a reasonable approximation.

Wu et al. (2019) first estimated the average gas velocity near the probe based on the gas volumetric flow rate and cross-sectional area of the OFC. They then employed the average particle velocity near the probe (V_p is assumed to be equal to the average gas velocity), in conjunction with the particle diameter (d_p), particle density (ρ_p), (estimated) gas viscosity (μ_p) and probe diameter (d_c) to calculate the particle Stokes numbers (Stk) of the fly-ash particles near the probe as:

$$Stk = \frac{\rho_p d_p^2 V_p}{9 \mu_g d_c} \tag{4}$$

The $\eta^{impaction}$ for each size range (i) were then computed according to the equation (Lokare et al. 2006):

$$\eta_i^{impaction} = [1 + 1.34(Stk - 0.1238)^{-1} + 0.034(Stk - 0.1238)^{-2} + 0.0289(Stk - 0.1238)^{-3}]^{-1} \tag{5}$$

The overall $\eta^{impaction}$ for each scenario was then computed as the fly-ash-mass-weighted averaged value of the $\eta^{impaction}$ across each size range (i):

Table 4 Parameters used for estimating Stk (Eq. (4)) and $\eta^{impaction}$ (Eq. (6)) when using the plug flow assumption (Ash density: 1300 kg/m³)

Case	Gas density (kg/m ³)	Gas viscosity (Pa s)	Gas velocity (m/s)
AIR	0.302	1.59×10^{-5}	0.73
OXY70	0.361	1.37×10^{-5}	0.28

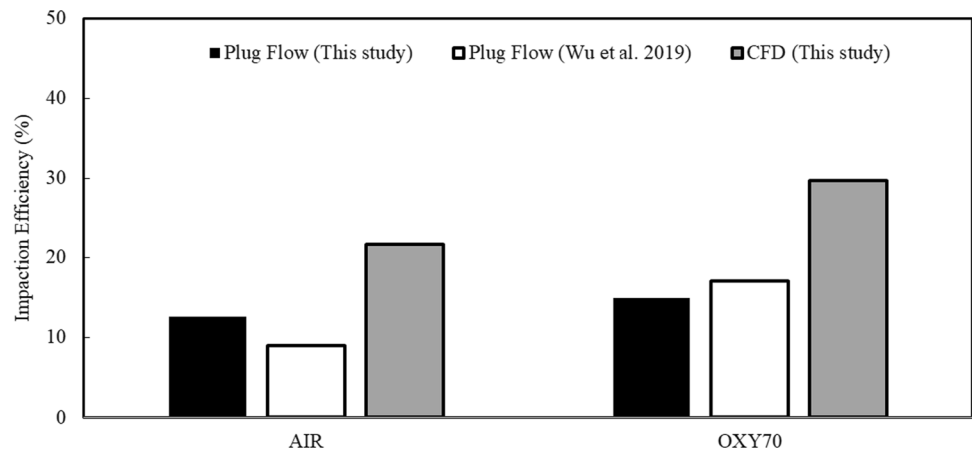
$$\eta^{impaction} = \frac{\sum m_i \eta_i^{impaction}}{\sum m_i} \tag{6}$$

where m_i is the mass-fraction of the fly-ash in each size range.

As a further validation of our computed CFD flow field, a plug flow based $\eta^{impaction}$ was calculated based on mass weighted averaged values of: gas velocity, gas density and gas viscosity near the probe obtained from the CFD simulations that are reported in Table 4. Figure 4 compares the plug flow based $\eta^{impaction}$ computed in this study against corresponding values reported by Wu et al. (2019). Good agreement between our predictions against those reported by Wu et al. (2019) leads further credence to the validity of the mass-weighted averaged flow variables (across the reactor cross-section) near the probe predicted by CFD. Any minor in $\eta^{impaction}$ between the two plug flow calculations

may be attributed to small gas property or velocity variations employed to compute the particle Stokes numbers (Stk) (Eq. (4)) between the two plug flow calculations. Overall, the volumetric flow rates of flue gas varied from 9 Nm³/h (OXY 70) to 29 Nm³/h (AIR) representing a threefold variation in magnitude. However, both sets of plug flow calculations show that in spite of the lower velocities in the OXY70 scenario, the impaction efficiencies actually increase due to the shift in ash PSD to larger diameters possibly resulting from increased coagulation and agglomeration due to higher temperatures and longer residence times. It is worth noting that an ash density of 1300 kg/m³ were used in both sets of plug flow calculations to enable consistency when

Fig. 4 Impaction efficiency predictions using plug flow and CFD methodologies



comparing the two sets of plug flow predictions. However, an ash density of 2500 kg/m^3 (coal ash) and 1700 kg/m^3 (for the more porous RH ash) was used in all of the CFD based deposition rate calculations as described in Sect. 2.2. These differences between the ash densities employed in the plug flow calculations and the CFD calculations in conjunction with the fact that CFD accounts for the spatial variations in the flow field near the probe (as opposed to employing an average velocity to compute Stk in Eq. (4)) are the primary reasons for the observed differences between the plug flow calculations and CFD calculations in Fig. 4.

2.2 Modeling particle impaction

Equations (4)–(6) demonstrate that getting the particle Stk right is pivotal to predicting accurate $\eta^{impaction}$ in the CFD calculations. However, due to the complex physio-chemical transformations undertaken by the particle prior to deposition, modeling the evolution of the fly-ash PSD (that matches the measured values near the probe) starting from the parent fuel PSD data alone is quite challenging. In addition to this, char combustion models provide users with only a limited ability to control particle densities and diameter during the burnout process (both of which influence the Stk) (ANSYS Fluent Theory Guide 2020). For instance, the kinetic/diffusion heterogeneous combustion model employed in this study, changes particle densities (ρ_p) as a result of mass loss but the particle diameter (d_p) remains invariant from that of the parent fuel. The intrinsic char combustion model (ANSYS Fluent Theory Guide 2020) on the other hand uses burning mode parameters (β) in well-known power law expressions to take into account variations in both particle density and diameter during burnout. However, β is a very fuel specific parameter, values of which may not be available for fuels under investigation (Kleinhans et al. 2018a).

In lieu of these shortcomings, a judiciously decoupled CFD methodology is adopted in this study where flow, heat transfer and ash deposition calculations were carried out downstream of the region where carbon burnout had been fully accomplished (cf. Figs. 1b and 2). This represented the radiation zone of the combustor. The fly-ash particles were injected into the inlet of the radiation zone as inert particles (Fig. 1b). In addition, the spatially varying profiles of all necessary field variables from the combustion simulation including gas velocities and temperature, turbulence variables and transport properties were transferred into the inlet boundary conditions of the radiation zone. This enabled us to specify both the correct fly ash PSD (d_p), particle densities (ρ_p), gas velocities and viscosities thereby enabling accurate predictions of Stk . The adequacy of this approach can be seen in Fig. 5 where the centerline temperature predictions along the axial length of the combustor between the fully coupled combustion calculation and the ash deposition simulations are compared. In this study, a constant density of 2500 kg/m^3 was assigned for the coal ash particles whereas the more porous RH ash was assigned a density of 1700 kg/m^3 .

2.3 Modeling particle capture

Models of various degrees of sophistication and fidelities have been developed over the years to represent the capture phenomena accurately and have been the subject of recent reviews (Kleinhans et al. 2018b; Cai et al. 2018). In this study, a critical particle viscosity based capture criterion was adopted where the capture probability (P_{stick}) equals unity if the particle viscosity (μ_p) is lower than a critical viscosity ($\mu_{p, critical}$):

$$P_{stick} = 1 \text{ if } \mu_p \leq \mu_{p, critical} \quad (7)$$

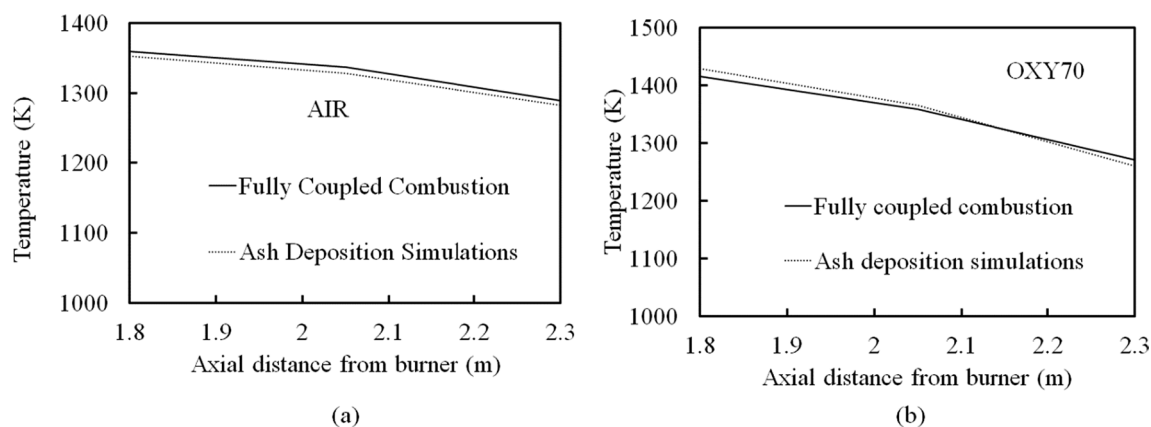


Fig. 5 Comparison of centerline temperature predictions along the axial length of the combustor between the fully coupled combustion calculation and the ash deposition simulations (probe location is at an axial distance of 2.3 m from the burner) **a** AIR **b** OXY70

Otherwise P_{stick} is zero. Based on three datasets associated with similar particle sizes, particle kinetic energy (PKE) and gas velocities associated with this study, the following relationship between PKE and critical viscosity ($\mu_{p,critical}$) proposed by Kleinhans et al. (2018b) was adopted:

$$\mu_{p,critical} = \frac{5 \times 10^{-12}}{PKE^{1.78}} \tag{8}$$

It is important to note that while this criterion was originally developed for silica rich soda lime glasses, its validity has been established for biomass ashes also by Schulze et al. (2007). In Fig. 6b, the sticking criterion (Eqs. (7) and (8)) represented as a function of particle viscosity and particle kinetic energy is represented as a diagonal line demarcating the sticking and rebounding conditions.

Two common correlations to model the compositional and temperature dependencies of the particle viscosity were

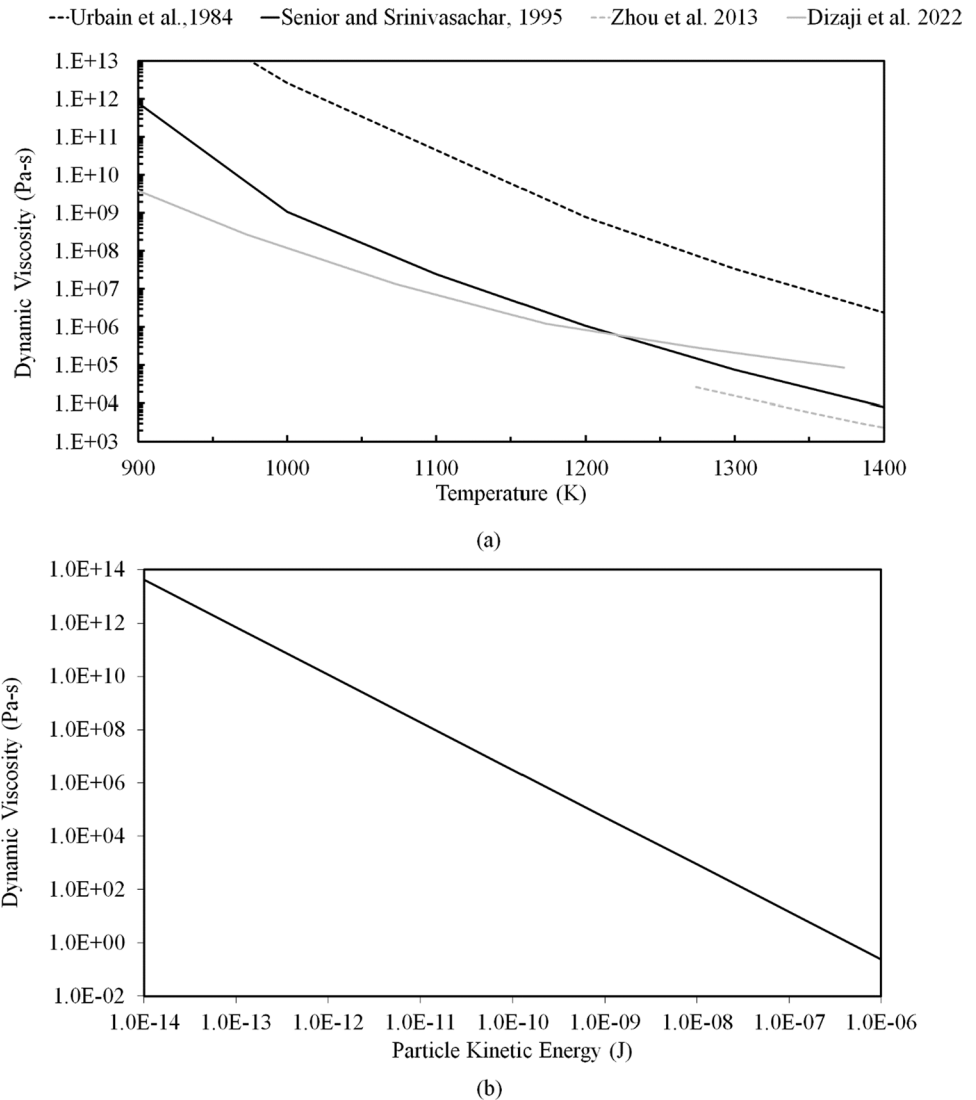
initially explored in this study. The first was the model proposed by Urbain summarized in (Urbain et al. 1982; Vargas et al. 2001) and second, the model proposed by Senior and Srinivasachar (1995). At the gas temperature range of interest in this study (1200–1300 K), the particle viscosity predicted by both models can differ by several order of magnitudes with the differences more profound for the silica rich RH ash as shown in Fig. 6a. Both models are presented here in a succinct manner:

The particle viscosity is a function of particle temperature T_p and two composition dependent model constants “A” and “B”

$$\mu = AT_p \exp\left(\frac{1000B}{T_p}\right) \tag{9}$$

The model constant “B” is first calculated from the mass fractions of different metal oxide (M_xO_y) constituents of the

Fig. 6 a RH ash viscosity predictions employing different models (Urbain et al. 1982; Senior and Srinivasachar (1995) **b** The sticking criterion (Eqs. (7) and (8)) represented as a function of particle viscosity (μ_p) and particle kinetic energy (PKE)



ash (Urbain et al. 1982; Vargas et al. 2001; Senior and Srinivasachar 1995):

$$B = f(M_x O_y) \quad (10)$$

where the metal oxide ($M_x O_y$) compositions of the bulk ash of the parent fuel (coal) were employed to estimate the constant B . The model constant “ A ” is then estimated from “ B ” using different functional forms as Senior and Srinivasachar (1995):

$$A = f(B, NBO/T) \quad (11)$$

here NBO/T is the ratio of non-bridging oxygen atoms (NBO) to the tetrahedral oxygen atoms in the glassy silica network of the ash. NBO/T was determined as a function of metal oxide ($M_x O_y$) compositions of the bulk ash of the parent fuel (coal). In the Senior and Srinivasachar (1995) model, two sets of constants A and B are computed corresponding to high temperature and low temperature data sets employed in their formulation. Correspondingly, two sets of particle viscosity (Eq. (9)) are initially computed for each particle when employing this model and the larger of the two values assigned to μ_p . While several studies have demonstrated the applicability of Senior and Srinivasachar (1995) viscosity correlations for the bituminous/sub-bituminous coal ashes similar to the coal ash investigated in this study, Fig. 6a shows that recent measurements of viscosities of the silica rich RH ash by Zhou et al. (2013) and Dizaji et al. (2022) are also shown to be in reasonable agreement those predicted by these correlations. Consequently, the Senior and Srinivasachar (1995) based viscosity correlations were employed in all of the deposition results reported in this study.

2.4 Modeling erosion/shedding caused by RH ash

While Wu et al. (2019) investigated three fuel types (Coal, Coal-RH and RH-Natural Gas), the RH fly ash was associated with erosion/shedding. This is also in agreement with the results from Qui et al. (2014) who showed that the addition of rice hull changed the microstructure of the deposits making them more porous and friable and easily removable by erosion. To model the erosion/shedding process induced by the RH fly-ash, the erosion model from Zhou and Hu (2021) was implemented and its associated equations are:

The energy before impact was determined as a sum of PKE and surface tension as:

$$E = \frac{\pi d_p^3 \rho_p u_p^2}{12} + \pi d_p^2 \gamma \quad (12)$$

The surface tension (γ) was modeled as:

$$\gamma = -0.0003T_p + 0.66 \quad (13)$$

The energy after impact (E') was computed as:

$$E' = \frac{\pi d_p^2 \gamma}{4} \left[d_m^2 (1 - F_a \cos \theta) + \frac{8}{3d_m} - D_e^2 \left(\frac{2}{1 + F_a \cos \theta} - F_a \cos \theta \right) \right] \quad (14)$$

θ and F_a represent the contact angle and the effective contact area respectively and D_e represents the potential spreading ratio:

$$D_e = \left[\frac{4 \sin \theta}{\tan^2 \theta (2 + \cos \theta)} \right]^{\frac{1}{3}} \quad (15)$$

As a first approximation a value of unity was assumed for the entire term within the bracket on the right hand side of Eq. (14) which corresponds to the assumption that the energy after impact was 25% of the surface tension component of the incoming energy. This is in reasonable approximation to the values used by Zhou and Hu (2021) where values of 67 degrees for θ and 0.95 for F_a were employed resulting in 20% of the surface tension component of the incoming energy remaining after impact. E and E' were then employed to compute the erosivity (e) (mass eroded over mass impacted) as:

$$e = \frac{0.05 d_{\text{dep}} (E - E')}{2\pi d_p^3 \gamma (1 - \sqrt[3]{1 - \xi_s})} \quad (16)$$

In this study, the diameter of the deposit (d_{dep}) was set to be equal to the diameter of the particle (d_p). Among the three modes of shedding (Zhou et al. 2013): gravity, erosive and thermal shock, the above equations represent the erosive shedding process. This is anticipated to be the main mode of shedding since the majority of the ash deposition was observed in the upper region of the probe facing the flow (Wang 2019). A molten slag fraction (ξ_s) of 0.15 was assumed in this study based on the FactSage calculations reported in Wu et al. (2019) at a temperature of 1300 K which is in reasonable agreement with the value reported in Zhou et al. (2013). This use of deposit composition based FactSage calculations thereby includes the effects of alkali/alkali earth metals (Potassium in particular) in the coal-biomass ash and their influence on the melting point. While the molten slag fraction did not change between AIR and OXY70, the use of additives can increase the melting points ash shown by Wang et al. (2020a, b).

Table 5 Impaction rate prediction (% Impaction efficiencies $\eta^{impaction}$ are also reported within brackets)

Fuel	Rice husk	Coal	Total
AIR (g/m ² h)	126 (27)	290 (12)	417 (14)
OXY70 (g/m ² h)	131 (28)	727 (30)	858 (30)
Impaction rate enhancement (OXY70/AIR)	1.04	2.50	2.06

Table 6 % Capture efficiencies ($\eta^{capture}$) and collection efficiencies ($\eta^{collection}$) prior to the inclusion of shedding

Sample	Capture efficiencies		Collection efficiencies	
	AIR	OXY70	AIR	OXY70
Rice husk	58	54	15	15
Coal	80	73	10	22
Total	73	70	11	21

3 Results and discussion

3.1 Impaction efficiencies

The overall impaction efficiency ($\eta^{impaction}$) was calculated as the ratio of the overall arrival rate of particles onto the deposition surface to the mass flux of the particles at the projected surface in front of the deposition surface as per Eq. (6). Table 5 and Fig. 4 show the $\eta^{impaction}$ as computed in the CFD calculations employing 200 bins to resolve the fly-ash PSD. Despite lower velocities in OXY70, the larger-sized particles contribute to increased impaction rates in comparison to AIR. The differences in the $\eta^{impaction}$ between the larger (but more porous) RH ash particles and the smaller coal ash particles was more evident in the AIR scenario than in the OXY70 scenario.

3.2 Capture and collection efficiencies

Collection efficiencies ($\eta^{impaction}$) were defined as:

$$\eta^{collection} = \frac{m_d A_p}{m_f x_f A_c} \tag{17}$$

where m_d is the mass of deposit collected on the probe, m_f is the mass of fuel fed into the furnace, x_f is the ash content of fuel, A_c is the projected area of the probe and A_p is the cross-sectional area of the OFC.

The capture efficiencies were then estimated from the predicted $\eta^{impaction}$ and $\eta^{collection}$ as:

$$\eta^{capture} = \frac{\eta^{collection}}{\eta^{impaction}} \tag{18}$$

Values of $\eta^{capture}$ and $\eta^{collection}$ variations are reported in Table 6. First, for a given fuel type the capture efficiencies are not different for AIR and OXY70 conditions indicating that the PKE plays a significant role in the capture process. This is in line with the conclusions draw by Wu et al. 2019 whose experiments are the basis of this study. However, a slightly lower capture efficiencies were observed for the non-sticky RH ash due to higher KE and higher viscosities

(Fig. 6) both of which increase the propensity to rebound as per our capture criterion (Eq. (7)).

3.3 Effect of erosion

Deposition rate predictions (with shedding) as well as the deposition rate enhancement (OXY70/AIR) are reported in Table 7 where the effects of mass removal by the more erosive RH ash particles were taken into account. The results are in good agreement with measured values (with shedding). Further, it is interesting to note that the predicted deposition rate ratios (OXY70/AIR) remain nearly unchanged with and without the use of the shedding model. This is attributed to the fact that shedding caused a correspondingly equal removal of the deposited ash (nearly 50%–60%) in both the AIR and OXY70 scenarios. This is likely due to similar PKE distributions between the RH ash particles in both scenarios shown in Fig. 6b. In spite of the lower velocities in the OXY70 scenario this results from the larger sized RH ash particles in OXY70 (Figs. 3a and b). This is also reflected in similar $\eta^{impaction}$ for the RH ash particles between the two scenarios as shown previously in Table 5. Given the important role played by the RH ash PKE in the ash shedding process, studies by Wang et al. (2019a, b) did indeed show that if the RH ash PSD was fine, it may not be able to induce shedding and mitigate ash deposition. In contrast, the coal ash particles have significantly different PKE distributions in Fig. 6a (with the OXY70 scenario exhibiting higher KE) which is also reflected in the significantly higher $\eta^{impaction}$ observed for the coal ash particles in the OXY70 scenario when compared to the AIR scenario (Fig. 7).

4 Conclusions

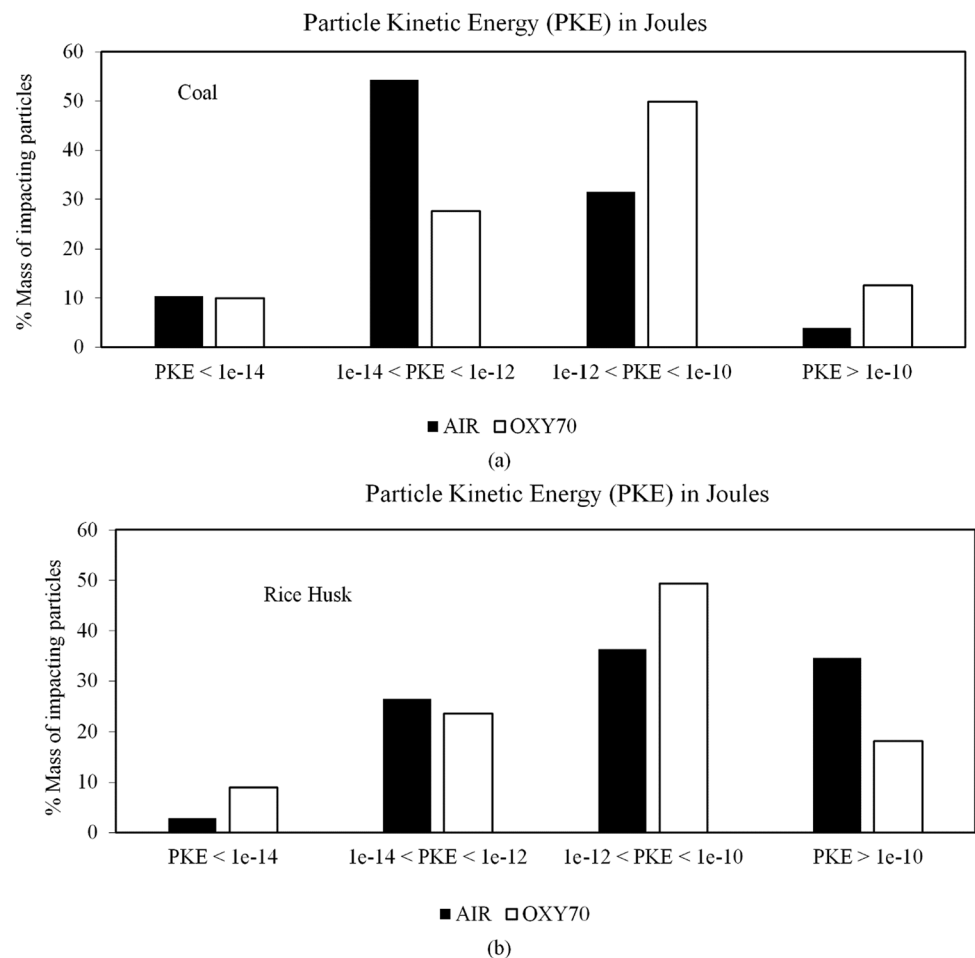
A Computational Fluid Dynamic (CFD) methodology where the combustion and ash deposition processes were judiciously “loosely” coupled to model the impaction accurately, in conjunction with add-on ash deposition and shedding modules, radiative property models applicable to low

Table 7 Deposition rate prediction ($\text{g}/\text{m}^2 \text{h}$) with and without shedding

Parameter	Measured (with shedding)	Predicted (with shedding)	Measured (prior to shedding onset)	Predicted (without shedding model)
AIR ($\text{g}/\text{m}^2 \text{h}$)	100*	131	100*	305
OXY70 ($\text{g}/\text{m}^2 \text{h}$)	250	290	700	600
Deposition rate enhancement (OXY70/AIR)	2.5	2.2	7.0	2.0

*Unlike the OXY70 scenario where shedding was reported after 30 min, Wu et al. (2019) reported that the weight of the deposits during AIR firing was increasing linearly with time

This could be due to the occurrence of a continuous shedding process or the coverage of the initial sticky ash layer with a loose RH ash deposit that suppresses deposit growth

Fig. 7 Histograms representing the kinetic energy distribution of the impacting particles **a** Coal ash **b** RH ash

$\text{H}_2\text{O}/\text{CO}_2$ environments were used to model the outer ash deposition and shedding rates measured during co-combustion of coal/RH in AIR and O_2/CO_2 (70/30 vol %, OXY70) oxidizer compositions. The following conclusions can be drawn from this study:

- (1) The predicted temperature and volumetric gas flow rates near the deposit probe agreed well with the measurements across all scenarios. The OXY70 scenarios were characterized by a 60%–70% reduction in volumetric flow rates. Concurring with experimental observations, the simulations also showed that complete carbon burnout had occurred prior to ash deposition and the gas temperature near the probe ranged from 1200 to 1300 K as observed during several experimental campaigns at similar firing conditions within this combustor.
- (2) The CFD predicted mass-weighted averaged values of: gas velocity, gas density and viscosity near the deposit probe were employed to compute impaction

- efficiencies ($\eta^{\text{impaction}}$) using the plug flow assumption. The computed plug-flow $\eta^{\text{impaction}}$ were indeed in good agreement with the plug-flow $\eta^{\text{impaction}}$ reported in the experimental study further ascertaining the validity of our simulated flow field. In spite of the lower flow rates associated with the OXY70 scenario, the larger fly-ash particles resulted in higher $\eta^{\text{impaction}}$ in comparison to the AIR firing scenario.
- (3) Profiles of flow field and turbulence variables following the burnout region and the measured fly-ash particle size distributions (PSD), ash densities were then employed as inlet boundary conditions to carry out ash deposition predictions in the region downstream of the burnout zone. This enabled an accurate representation of ash density, ash PSD as well as $\eta^{\text{impaction}}$. The validity of this judiciously, loosely coupled approach was established by comparing the predicted flow fields near the probe obtained from the fully coupled combustion simulations and the deposition rate simulations. In concurrence with the plug flow calculations, the CFD predictions also showed higher $\eta^{\text{impaction}}$ associated with the OXY70 scenario. However, the values of $\eta^{\text{impaction}}$ were different due to a more accurate representation of the flow field surrounding the probe geometry and a finer resolution associated with the fly-ash PSD (200 bins).
 - (4) The differences in the $\eta^{\text{impaction}}$ between the larger (but more porous) RH ash particles and the smaller coal ash particles was more evident in the AIR scenario than in the OXY70 scenario. Further, the $\eta^{\text{impaction}}$ ratio (OXY70/AIR) was similar to the $\eta^{\text{collection}}$ ratio (OXY70/AIR) indicating that similar η^{capture} likely prevailed in the AIR and OXY70 scenarios. This is in line with the conclusions draw by Wu et al. (2019) whose experiments are the basis of this study.
 - (5) A recently proposed particle kinetic energy (PKE), critical viscosity (μ_{critical}) and particle viscosity (μ_p) based ash capture criterion that was originally developed for silica rich soda lime glasses but whose validity for biomass ashes has also been established was implemented to model the ash capture process. To compute μ_p associated with the widely varying coal and RH fly-ash compositions, two common fly ash composition and temperature based viscosity correlations were identified (Urbain et al. 1982; Senior and Srinivasachar 1995) and evaluated for their applicability to model the deposition process in this scenario. Given the temperature range of interest for the deposition process in this study (1200–1300 K), the Senior and Srinivasachar (1995) model was deemed to be more applicable for the coal as well as RH ashes.
 - (6) The proposed capture criterion did indeed confirm that nearly identical η^{capture} (50%, 73%) prevailed in the AIR and OXY70 scenarios respectively. However, the more viscous coal ash particles had slightly a higher η^{capture} (73%–80%) compared to the non-sticky RH ash (54%–58%). Since the chemical and physical interactions among the two fuel ashes were neglected in these calculations (i.e., each ash particle was based on its parent fuel composition and was assumed to impact and deposit independent of the presence of any other ash particle), the results show that the deposition characteristics in the measurements of Wu et al. (2019) were likely dominated by PKE effects.
 - (7) In addition, a recently proposed erosion/shedding model that takes the deposit melt fraction (η_s), the energy consumed during particle impact and surface tension effects into account was also implemented and shedding due to the more erosive RH ash particles were calculated. Deposition rate predictions (with shedding) as well as the deposition rate enhancement (OXY70/AIR) were in good agreement with measured values (with shedding). Nearly, 50%–60% of the deposited ash was removed by the shedding process in both the AIR and OXY70 scenarios. This is likely due to similar PKE distributions between the RH ash particles in both scenarios that resulted in similar shedding rates.
- The implications of this research extend to second generation oxy-combustion and load following operations that are accompanied by a significant (60%–70%) reduction in combustor flue gas flow rates when compared to baseload operation. Decrease in velocities (and particle Stokes numbers) may cause a corresponding decrease in impaction efficiencies, deposition and shedding rates. On the other hand, longer residence times associated with these velocity reductions may promote particle interactions/agglomeration resulting in a larger-sized fly-ash PSD which in turn may *increase* the impaction efficiencies, deposition and shedding rates.

Funding This research was funded through the University Coal Research Program being administered by DOE-NETL (Award Number: DE-FE0031741).

Availability of data and materials All data relevant to this research are reported in the manuscript.

Declarations

Conflict of Interests The author declares no conflict of interests.

Open Access This article is licensed under a Creative Commons Attribution 4.0 International License, which permits use, sharing, adaptation, distribution and reproduction in any medium or format, as long as you give appropriate credit to the original author(s) and the source, provide a link to the Creative Commons licence, and indicate if changes were made. The images or other third party material in this article are

included in the article's Creative Commons licence, unless indicated otherwise in a credit line to the material. If material is not included in the article's Creative Commons licence and your intended use is not permitted by statutory regulation or exceeds the permitted use, you will need to obtain permission directly from the copyright holder. To view a copy of this licence, visit <http://creativecommons.org/licenses/by/4.0/>.

References

- ANSYS, Inc. ANSYS Fluent Theory Guide (2020). Release 20.1.
- Cai Y, Tay K, Zheng Z, Yang W, Wang H, Zeng G, Li Z, Boon SK, Subbaiah P (2018) Modeling of ash formation and deposition processes in coal and biomass fired boilers: a comprehensive review. *Appl Energy* 230:1447–1544
- Chao CY, Kwong PC, Wang JH, Cheung CW, Kendall G (2008) Co-firing coal with rice husk and bamboo and the impact on particulate matters and associated polycyclic aromatic hydrocarbon emissions. *Bioresour Technol* 99:83–93
- Dizaji HB, Zeng T, Hölzig H, Bauer J, Klöß G, Enke D (2022) Ash transformation mechanism during combustion of rice husk and rice straw. *Fuel* 307:121768
- Schulze K, Hofmeister G, Joeller M, Scharler R, Obernberger I, Korbee R, Cieplik M, (2007) Development and evaluation of a flexible model for CFD simulation of ash deposit formation in biomass fired boilers. In: Proceedings of the International Conferences “Impacts of Fuel Quality on Power Production”, EPRI report (No. 1014551, pp 7–95).
- Fakourian S, McAllister Z, Fry A, Wang Y, Li X, Wendt JO, Dai J (2021) Modeling ash deposit growth rates for a wide range of solid fuels in a 100 kW combustor. *Fuel Process Technol* 217:106777
- Gopan A, Verma P, Yang Z, Axelbaum RL (2020) Quantitative analysis of the impact of flue gas recirculation on the efficiency of oxy-coal power plants. *Int J Greenh Gas Control* 95:102936
- Krishnamoorthy G, Caitlyn W (2015) Assessing the role of particles in radiative heat transfer during oxy-combustion of coal and biomass blends. *J Combust*.
- Kleinhans U, Halama S, Spliethoff H (2018a) Char particle burning behavior: experimental investigation of char structure evolution during pulverized fuel conversion. *Fuel Process Technol* 171:361–373
- Kleinhans U, Wieland C, Frandsen FJ, Spliethoff H (2018b) Ash formation and deposition in coal and biomass fired combustion systems: progress and challenges in the field of ash particle sticking and rebound behavior. *Progr Energy Combust* 68:65–168
- Krishnamoorthy G (2013) A new weighted-sum-of-gray-gases model for oxy-combustion scenarios. *Int J Energy Res* 37(14):1752–1763
- Kwong PC, Chao CY, Wang JH, Cheung CW, Kendall G (2007) Co-combustion performance of coal with rice husks and bamboo. *Atmos Environ* 41(35):7462–7472
- Lokare SS, Dunaway JD, Moulton D, Rogers D, Tree DR, Baxter LL (2006) Investigation of ash deposition rates for a suite of biomass fuels and fuel blends. *Energy Fuels* 20(3):1008–1014
- Qiu K, Zhang H, Zhou H, Zhou B, Li L, Cen K (2014) Experimental investigation of ash deposits characteristics of co-combustion of coal and rice hull using a digital image technique. *Appl Thermal Eng* 70(1):77–89
- Senior CL, Srinivasachar S (1995) Viscosity of ash particles in combustion systems for prediction of particle sticking. *Energy Fuels* 9(2):277–283
- Urbain G, Bottinga Y, Richet P (1982) Viscosity of liquid silica, silicates and aluminosilicates. *Geochim Cosmochim Acta* 46(6):1061–1072
- Vargas S, Frandsen FJ, Dam-Johansen K (2001) Rheological properties of high-temperature melts of coal ashes and other silicates. *Prog Energ Combust* 27(3):237–429
- Wang Y, Li X, Wendt JO (2019a) On ash deposition rates from air and Oxy-Combustion of pulverized coal, petroleum coke, and biomass. *Energy Fuels* 33(7):5849–5858
- Wang Y, Wu J, Li X, Han J, Yu D, Xu M, Wendt JO (2019b) Comparison study of ash partitioning and deposition behavior between two rice husk fuels under a 100 kW combustor. *Energy Fuels* 33(11):11968–11975
- Wang C, Bi H, Jiang X, Jiang C, Lin Q (2020a) Experimental study on ignition and combustion of coal-rice husk blends pellets in air and oxy-fuel conditions. *J Energy Inst* 93(4):1544–1558
- Wang Q, Han K, Wang P, Li S, Zhang M (2020b) Influence of additive on ash and combustion characteristics during biomass combustion under O₂/CO₂ atmosphere. *Energy* 195:116987
- Wang Y (2019) Ash aerosol and ash deposit formation during high temperature oxy-combustion of various solid fuels. In: University of Utah, PhD Dissertation.
- Weber R, Schaffel-Mancini N, Mancini M, Kupka T (2013) Fly ash deposition modelling: requirements for accurate predictions of particle impaction on tubes using RANS-based computational fluid dynamics. *Fuel* 108:586–596
- Wu J, Yu D, Zeng X, Yu X, Han J, Wen C, Yu G (2018) Ash formation and fouling during combustion of rice husk and its blends with a high alkali Xinjiang coal. *Energy Fuels* 32(1):416–424
- Wu J, Wang Y, Han J, Li X, Yu D, Xu M, Wendt JO (2019) Ash formation and deposition in oxy-fuel combustion of rice husk, coal, and their blend with 70% inlet O₂. *Energy Fuels* 34(1):890–899
- Yang L, Wang H, Zhu J, Sun W, Xu Y, Wu S (2022) Co-combustion and ash characteristics of Zhundong coal with rice husk hydrochar prepared by the hydrothermal carbonization technology for co-combustion. *IET Renew Power Gener* 16(2):329–338
- Yu D, Yu X, Wu J, Han J, Liu F, Pan H (2021) A comprehensive review of ash issues in oxyfuel combustion of coal and biomass: mineral matter transformation, ash formation, and deposition. *Energy Fuels* 35(21):17241–17260
- Zhan Z, Fry AR, Wendt JO (2016) Relationship between submicron ash aerosol characteristics and ash deposit compositions and formation rates during air-and oxy-coal combustion. *Fuel* 181:1214–1223
- Zhou H, Hu S (2021) Numerical simulation of ash deposition behavior with a novel erosion model using dynamic mesh. *Fuel* 286:119482
- Zhou H, Zhang H, Li L, Zhou B (2013) Ash deposit shedding during co-combustion of coal and rice hull using a digital image technique in a pilot-scale furnace. *Energy Fuels* 27(11):7126–7137
- Zhou M (2019) Large-Eddy simulation of near-wall multiphase flow in combustion systems. In: University of Utah, PhD Dissertation.

Publisher's Note Springer Nature remains neutral with regard to jurisdictional claims in published maps and institutional affiliations.